ACS APPLIED MATERIALS & INTERFACES

Research Article

www.acsami.org

Nanosphere Monolayer on a Transducer for Enhanced Detection of Gaseous Heavy Metal

Ylias M. Sabri,[†] Ahmad Esmaielzadeh Kandjani,[†] Samuel J. Ippolito, and Suresh K. Bhargava*

Centre for Advanced Materials and Industrial Chemistry (CAMIC), School of Applied Sciences, RMIT University, GPO Box 2476V, Melbourne, Victoria 3001, Australia

Supporting Information

ABSTRACT: This study reports for the first time that polystyrene monodispersed nanosphere monolayer (PS-MNM) based Au (Au-MNM) and Ag (Ag-MNM) nanostructures deposited on quartz crystal microbalance (QCM) transducers can be used for nonoptical based chemical sensing with extremely high sensitivity and selectivity. This was demonstrated by exposing the Au-MNM and Ag-MNM based QCMs to low concentrations of Hg^0 vapor in the presence interferent gas species (i.e., H_2O, NH_3, volatile organics, etc.) at operating temperatures of 30 and 75 °C. At 30 °C, the Au-MNM and Ag-MNM based QCMs showed ~16 and ~20 times higher response magnitude toward Hg^0 vapor concentration of 3.26 mg/m^3 (364 parts per billion by volume (ppb_v)) relative to their unmodified control counterparts, respectively. The results indicated that the extremely high sensitivity was not due to the increased surface area (only 4.62 times increase) but due to their long-range interspatial order and high number of surface defect formation which are selectively active toward Hg^0 vapor sorption. The Au-MNM and Ag-MNM also had more than an order of magnitude lower detection limits (<3 ppb_v) toward Hg^0 vapor compared to their unmodified control counterparts (>30 ppb_v). When the operating temperature was increased from 30 to 75 °C, it was found that the sensors exhibited lower drift, better accuracy, and better selectivity toward Hg^0 vapor but at the compromise of higher detection limits. The high repeatability (84%), accuracy (97%), and stability of Au-MNM in particular make it practical to potentially be used as nonspectroscopic based Hg^0 vapor sensor in many industries either as mercury emission monitoring or as part of a mercury control feedback system.

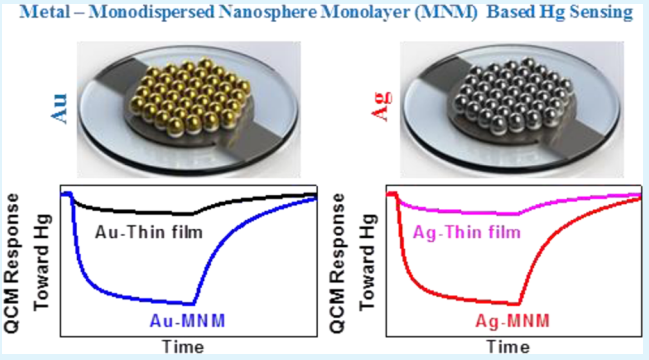

KEYWORDS: *photonic crystals, mercury emission monitoring, quartz crystal microbalance (QCM), polystyrene nanospheres, self-assembled monolayers*

1. INTRODUCTION

Nanoparticles are well-known for their enhanced physical and chemical properties over their bulk counterparts with the added possibility to manipulate these properties for a range of different applications by simply varying their dimension and geometry.[1,2] The integration of nanoparticles into one-, two-, or three-dimensional (2D or 3D) structures leads to novel collective properties that can be controlled by altering the nanoparticles' arrangements, which in turn influences their cooperative interactions.[3−5] Therefore, the development of functional nanostructures with specific patterns and high interstitial long-range order has received considerable interest in recent years due to their applications in the fields of solar cells, optical devices, chemical sensing, and catalysis.[6] From a chemical sensing point of view, it is important to consider not only high sensitivity but also uniformity and reproducibility of the surface (sensitive layer) itself. Typically, well-ordered nanostructures are fabricated using "top−down" methods such as focused ion beam (FIB)[7] and electron beam lithography (EBL).[8] However, the crystal structure or chemical properties of developed nanostructures could get damaged during the etching process. In addition, using these methods to fabricate nanostructures over a large substrate area is an expensive and time-consuming process. An alternative method is the self-assembly of polystyrene (PS) spheres that act as templates to fabricate periodic nanostructures. Templating has been widely used to produce a variety of devices taking advantages of its good reproducibility, large-scale uniformity (with less than 10% variation over the entire substrate), fast processing, high stability, large area, and low fabrication cost.[9−12] By use of this method, a lot of inorganic, organic, and metallic based ordered materials with various photonic crystal (PC) based structures have successfully been made as optical filters, nanolasers, waveguides, catalysts, chemical sensors, semiconductors, and microelectronics as well as telecommunication technologies, just to name a few.[12−16] In

Received: September 16, 2014
Accepted: January 6, 2015
Published: January 6, 2015

DOI: 10.1021/am507069z
ACS Appl. Mater. Interfaces 2015, 7, 1491−1499

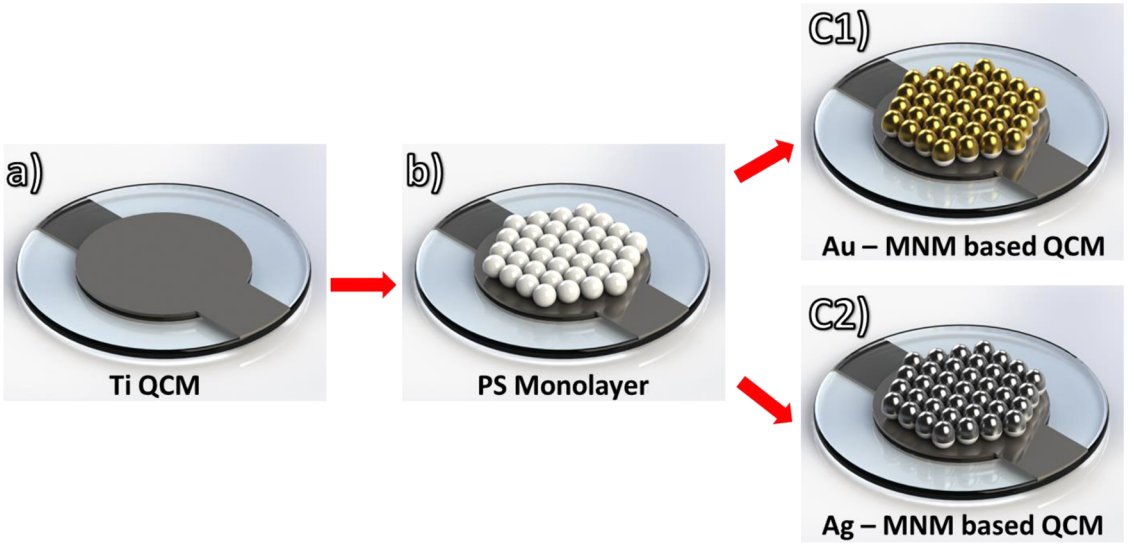

Figure 1. Representative schematic of the QCM modification process (a) e-beam evaporation of Ti electrodes on quartz substrates to form Ti QCMs followed by (b) transfer of self-assembled PSNSs on the Ti QCM followed by (c) e-beam evaporation of noble metals to form (c1) Au-MNM and (c2) Ag-MNM directly on the Ti electrode of QCM transducers.

particular, PCs are promising platforms that enable harnessing of increased sensitivity, better repeatability, and reduced noise in chemical sensing applications.[14] Further, the distance between the unit cells (i.e., spheres, cubes, etc.) in PCs can be controlled to govern their properties such as controlling the distinct wavelengths of reflection and color.[16,17] These features have made PC structures attractive in applications like surface enhanced Raman spectroscopy (SERS) based chemical sensing[12] where the close distance between the metal spheres (with PS nanosphere templates) results in the formation of electromagnetic hot spots,[18,19] thus enabling high sensitivities to be reached.

One of the most sought-after chemical sensors being developed among the scientific community is for anthropogenic elemental mercury (Hg^0) vapor detection.[20−24] The ever-growing efforts to develop a Hg^0 vapor sensor is partly due to the United Nations' environmental programme's (UNEP) recent Minamata Convention where delegates from 140 nations agreed on a legally binding rule on reducing anthropogenic mercury emissions.[25−27] This is not surprising when an estimated 60 000 babies with mercury related diseases are born in the U.S. alone each year because pregnant mothers are being exposed to mercury through their environmental surroundings or via consumption of contaminated food sources.[28,29] In order to reduce emissions, accurate, cheap, and reliable online Hg^0 monitoring technologies are imperative for providing feedback to industrial process control systems.[30] The conventional spectroscopic based instruments currently being used to detect mercury in industrial processes and emission points are either expensive, encounter problems with portability, require sample pretreatment, have cross-interference issues with other gas species present in the effluent gas, or have long turn-around times.[30−33] These shortcomings associated with spectroscopic based mercury detectors have shifted attention toward developing Hg^0 vapor sensors based on other mechanisms with particular attention given to microsensors.[20,21,23,34−36] However, thus far, producing a microsensor that addresses all of these shortcomings of spectroscopic based instruments has been met with limited success. Most of the sensors developed are plagued by their low sensitivity, low temperature stability, and lack of selectivity toward Hg^0 vapor. In this work, polystyrene monodispersed nanosphere monolayer (PS-MNM) based Au (Au-MNM) and Ag (Ag-MNM) are deposited on quartz crystal microbalance (QCM) transducers and compared for their sensitivity and selectivity toward low concentrations of Hg^0 vapor. The selectivity of the sensors toward Hg^0 vapor was determined by simultaneously introducing high humidity and ammonia content as well as other volatile organic compounds (VOCs), which are highly abundant in most industrial processes and/or have high affinity toward noble metal nanostructures. The MNM based microsensor demonstrated in this work can potentially be used in harsh industrial process as a small, independent, reliable, and sustainable unit to monitor Hg^0 vapor in stack gas as well as operate as part of Hg^0 vapor emissions control systems.

2. EXPERIMENTAL SECTION

Figure 1 shows a summary of the MNM based QCM transducer fabrication process. Briefly, a 300 nm Ti layer was deposited on optically polished AT-cut quartz substrates using e-beam evaporation on both sides of the substrates (Figure 1a). To achieve polystyrene nanospheres (PSNSs) based MNM on the prepared QCMs, initially ∼500 nm PSNSs were synthesized using dispersion polymerization method. The PSNSs were then used to form a monolayer template on the transducers via air/water interface self-assembly (Figure 1b). A 100 nm Au (Figure 1c1) or Ag (Figure 1c2) layer was then deposited on the modified QCMs using e-beam evaporation in order to form the Au-MNM or Ag-MNM directly on the QCM transducers. All chemicals used in this work were purchased from Sigma-Aldrich and used as received. The quartz crystals (10 MHz, AT-cut, polished) were purchased from AATA, Japan.

2.1. Polystyrene Nanoparticle Synthesis. The polystyrene nanospheres (PSNSs) were synthesized using dispersion polymerization method described by Unciti-Broceta et al.[37] Briefly, a 20 mL styrene monomer was first washed with ammonia (28%) solution to remove any inhibitor that may have been present in the monomer solution. The monomer was then washed with Milli-Q water (resistivity of 18.2 MΩ·cm, Millipore) several times until a pH of 7 was attained. Then 2 mL of the washed styrene was dissolved in 18 mL of ethanol solution containing 20% water. The process was performed in a three-neck round-bottom flask which was purged with dry

DOI: 10.1021/am507069z
ACS Appl. Mater. Interfaces 2015, 7, 1491−1499

nitrogen to remove any oxygen and therefore avoid unwanted polymerization. Approximately 800 mg of polyvinylpyrrolidone (PVP) was then dissolved in the prepared solution. Thereafter the mixture was added to the monomer solution as a steric surfactant and heated to 70 °C while stirring at 1500 rpm. In order to start the polymerization reaction, 28 mg of azobisisobutyronitrile (AIBN) initiator was dissolved in 20 mL of ethanol, purged with dry nitrogen gas for 10 min, and finally injected to the prepared solution. The synthesis was performed under dry N_2 atmosphere, while the temperature and stirring were kept constant for a period of 24 h. This method produced the PSNSs of 500 ± 50 nm. The formed PS monodispersed particles were centrifuged and washed with ethanol and water several times and redispersed in ethanol.

2.2. QCM Fabrication. The QCM transducer relies on measuring the resonant frequency (f_0) of the QCM upon exposure to the gas stream containing Hg^0 vapor. Given that the sensitive layer on the QCM electrodes has high affinity and is very selective toward Hg^0 vapor, an amalgam will be formed when Hg^0 vapor comes into contact with the sensor surface, thus resulting in increased mass of the QCM electrodes. From Sauerbrey's equation,[38] a change in mass (Δm) of the electrodes results in a proportional change in the resonant frequency (Δf) of the QCM as

$$\Delta f = -S_f \Delta m \quad (1)$$

where S_f represents the integral mass sensitivity (or Sauerbrey constant). In order to fabricate the QCM transducers, a 300 nm Ti layer was deposited on optically polished AT-cut quartz substrates (⌀ 7.5 mm, 10 MHz resonant frequency, Hy-Q Crystals, Australia) using e-beam evaporation on both sides of the substrate. The Ti layer was used as the QCM electrodes because of its high adhesion properties to quartz as well as its lack of affinity toward Hg^0 vapor.[39,40]

2.3. Au-MNM and Ag-MNM Based QCM Fabrication. The Ti based QCM electrodes (⌀ 4.5 mm) were modified by employing the widely used self-assembly process to form a monolayer of PSNSs,[41] hence direct formation of PS-MNM on QCM transducers. Briefly, the synthesized PSNSs were first suspended in ethanol. A few drops (~10 μL) of the suspension were then introduced on the water surface inside a glass Petri dish which had an internal diameter of 10 cm. Introduction of PS solutions was stopped when about $^3/_4$ of the water surface was covered with PSNS. A few drops of sodium dodecyl sulfate (SDS, $NaC_{12}H_{25}SO_4$) were then added in the Petri dish to form rigid, close-packed PSNS monolayers through the modification of the water surface tension. PSNS monolayer array was transferred from the water surface to the surface of the Ti based QCM electrode by simply dipping the quartz substrates (⌀ 7.5 mm) in the solution and removing it gently over a period of 30 s. The QCMs were then left to dry under N_2 atmosphere. A 100 nm Au or Ag layer was then deposited on the modified QCMs using e-beam evaporation on both sides of the substrate in order to form either Au-MNM or Ag-MNM based QCM. In order to fabricate the control QCMs, a 100 nm Au (referred to as Au-control) or Ag (referred to as Ag-control) layers were also deposited on the Ti based QCMs. The metal depositions were performed by a Balzers e-beam (BAK 600) at room temperature (~22 °C) and typical base pressure of 2×10^{-7} mbar. The Ti, Au, and Ag layers were deposited at 0.1, 0.2, and 0.2 nm/s deposition rates, respectively. The electron beam evaporator was set at an electron beam voltage of 6 keV for Ti and Ag or 11 keV for Au.

2.4. Surface Characterization. Following their modification, the QCMs were first characterized using scanning electron microscopy (SEM) on a Nano-SEM instrument operating at an accelerating voltage of 10 kV. X-ray photoemission spectroscopy (XPS) of the surfaces was then carried out using Thermo K-Alpha XPS instrument which had a Mg Kα radiation source at a pressure better than 1×10^{-9} Torr and with a spectral resolution of 0.1 eV. The elemental binding energies (BEs) were aligned to the adventitious C 1s BE of 285 eV.

Electrochemical Surface Area. The electrochemical surface area (ESA) of Au-MNM was determined using the linear sweep voltammetry (LSV) technique. This process was first described by Rand and Woods[42] and involves calculating the charge required to reduce an oxide monolayer that is formed on the surface. The experiment consisted of performing cyclic voltammetry (CV) of both the control and modified surfaces at 100 mV s^{-1} in a 1 M H_2SO_4 solution. Although the LSV technique is not designed to estimate the ESA of silver sufaces, the Ag-MNM was assumed to have a similar ESA to that of Au-MNM due to their similarity in terms of metal film thickness and the underlying PSNS template.

2.5. Hg^0 Vapor Sensing Using Photonic Crystal Based QCMs. Both Au-MNM and Ag-MNM based QCMs as well as their unmodified control counterparts were tested for their sensing capabilities toward a dynamic range of mercury vapors at operating temperatures of 30 and 75 ± 1 °C to demonstrate the high sensitivity and selectivity of the modified sensors over their control counterparts. The operating temperature of 30 °C was used, as it was the closest to room temperature which could be controlled by the in-house built mercury vapor delivery system. On the other hand, 75 °C was chosen because this was near the temperatures used in field sampling of trace amounts of Hg^0 vapor in industrial effluents[43] and yet lower than the glass-transition temperature of polystyrene (~100 °C)[44] based template on the sensor sensitive layers. The mercury concentrations toward which the sensors were tested are 0.21, 0.31, 0.45, 0.64, 0.93, 1.27, 1.74, 2.38, and 3.26 ± 0.05 mg/m^3 where 1 mg/m^3 is equivalent to 111.7 ppb_v. The different concentrations of Hg^0 vapor were generated in a controlled manner using NIST certified mercury permeation tubes (VICI, TX, USA). Hg^0 vapor concentrations in the test stream were confirmed by using an acidic $KMnO_4$ impinger train calibration system (similar to the Ontario-Hydro method) and employing inductively coupled plasma mass spectroscopy (ICP-MS, Agilent 7700 series, ShieldTorch system) for their analysis. Two research quartz crystal microbalance (RQCM, Maxtek) units with a frequency resolution of ±0.03 Hz were used to measure the resonant frequency (f) of the four QCMs tested at any one time.

The sensors were tested continuously for a total of 25 days. All sensing measurements were conducted using the following procedure: The experiments were performed in a custom built gas cell, which housed four QCM sensors (Au-MNM modified, Ag-MNM modified, Au-control, and Ag-control), and exposed to a gas stream containing a mixture of dry N_2 and a known concentration of Hg^0 vapor (with or without interferent gases) for 1 h. Thereafter, the sensors were recovered by dry N_2 flow for 1 h without altering the total flow in the gas cell or the operating temperatures. The total flow of 200 standard cubic centimeters per minute (sccm) was kept constant using a specially developed multichannel gas delivery system, employing mass flow controllers (MKS instruments, Inc., USA). The sensors were tested toward Hg^0 vapor in the presence of additional interferent gases (ammonia, (NH_3, 384 ppm), acetaldehyde (Ac-ald, 304 ppm), ethyl mercaptan (Ethyl-M, 2.61 ppm), dimethyl disulfide (DMDS, 5.01 ppm), methyl ethyl ketone (MEK, 40.1 ppm), and humidity (H_2O, 27.2 g/m^3)) which are known for their extreme affinity for Au[21,45−54] or are common in many industrial effluents.[55] The high level of humidity (27.2 g/m^3) was generated using a relative humidity generator (V-Gen from InstruQuest).

3. RESULTS AND DISCUSSION

3.1. Surface Characterization of the Sensitive Layers. The SEM images of the Au-MNM and Ag-MNM are presented in Figure 2. The SEM images presented in Figure 2a1 and Figure 2a2 show the Au-MNM's monodispersion and surface coverage on the Ti electrode surfaces of the QCM transducers, respectively. Similarly, Figure 2b1 and Figure 2b2 show the Ag-MNM's monodispersion and surface coverage on the Ti electrode surfaces of the QCM transducers, respectively. It can be observed that highly monodispersed, hexagonally close-packed nanosphere monolayer of PSNSs are obtained on the QCM electrodes with long-range ordering on the Ti surface. Even though the PC (in this case metal-MNM) surfaces exhibit high surface to volume ratio, have relatively large number of active sites, and have shown excellent optical properties and SERS based sensing activities in the past,[9,41,56,57] they have not

DOI: 10.1021/am507069z
ACS Appl. Mater. Interfaces 2015, 7, 1491−1499

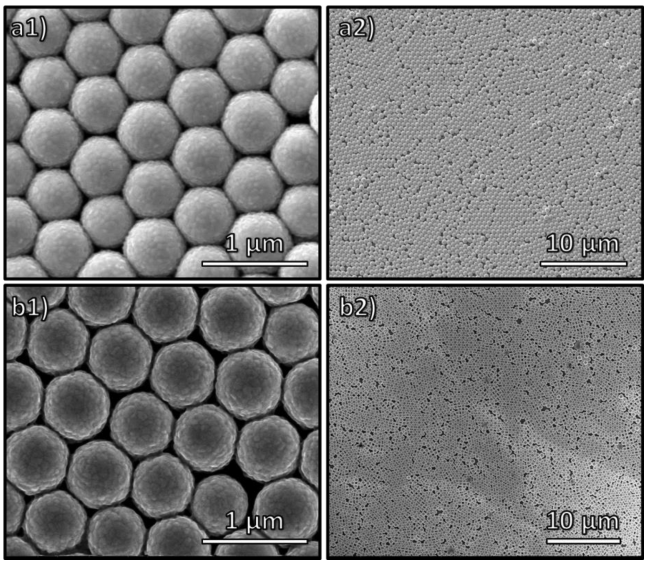

Figure 2. SEM images representing (a1) close-packed Au-MNM, (a2) surface coverage of Au-MNM on the Ti electrode of QCM transducer, (b1) close-packed Ag-MNM, and (b2) surface coverage of Ag-MNM on the Ti electrode of QCM transducer.

yet been tested for nonoptical based Hg^0 vapor sensing applications. It is envisaged that the spherical shape of the PSNSs combined with their close packed arrangement will produce active sites (following metal deposition) that will have high sensitivity toward Hg^0 vapor. In addition to high sensitivity, high selectivity is expected to be achieved by choosing the appropriate material with high affinity solely toward Hg^0 vapor.

In order to determine the increase in surface area of the modified surfaces over the control substrate that resulted because of MNM formation, the active electrochemical surface areas (ESAs) of the Au-control and Au-MNM were determined using the linear sweep voltammetry (LSV) technique[42] as shown in Figure 3. As expected, the ESA increased with the formation of MNM with the ratio of the Au-MNM to Au-control ESA being about 4.62 and therefore should achieve at least a similar increase in response magnitude toward Hg^0 vapor.

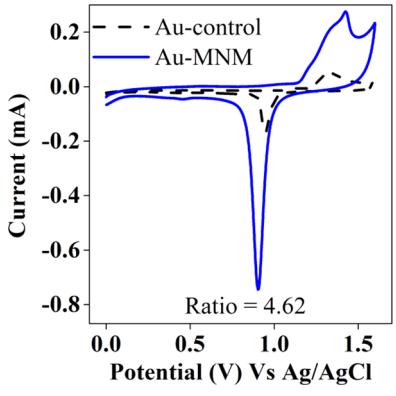

Figure 3. Linear sweep voltammograms (LSVs) obtained at 100 mV s^{-1} in 1 M H_2SO_4 solution vs Ag/AgCl reference electrode for the Au-control and Au-MNM surfaces. The electrochemical surface area (ESA) was calculated from the reduction peak area, and the ratio of Au-MNM to Au-control was found to be 4.62.

3.2. Sensor Performance. In order to test the influence of operating temperature on the sensor response times, sensitivity, and detection limits, all four QCMs (Au-control, Ag-control, Au-MNM, and Ag-MNM) were exposed toward a set of Hg^0 vapor concentrations (0.21, 0.31, 0.45, 0.64, 0.93, 1.27, 1.74, 2.38, and 3.26 ± 0.05 mg/m^3) in sequential order from lowest to highest concentrations at operating temperatures of 30 and 75 °C. The sensor dynamic response at 30 and 75 °C are presented in Figure 4a1 and Figure 4b1, respectively, while

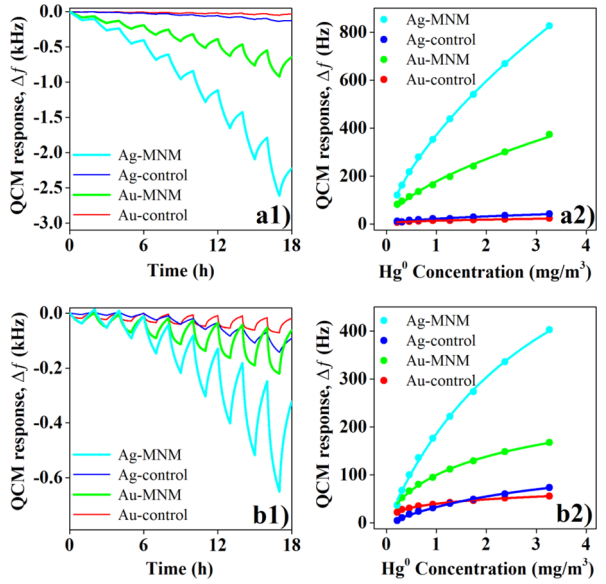

Figure 4. Modified (Au-MNM and Ag-MNM) and control (Au-control and Ag-control) based QCMs (a1) dynamic response, (a2) response magnitudes at 30 °C, and (b1) dynamic response, (b2) response magnitudes at 75 °C when exposed toward Hg^0 vapor concentrations of 0.21, 0.31, 0.45, 0.64, 0.93, 1.27, 1.74, 2.38, and 3.26 ± 0.05 mg/m^3 in sequential order from lowest to highest concentrations. The lines through the data points in (a2) and (b2) represent the lines of best fit for the LRC equation.

their corresponding analysis curves are shown in Figure 4a2 and Figure 4b2, respectively. It can be observed that the modified sensors have significantly more affinity toward Hg^0 vapor than their control counterparts at both operating temperatures. At 30 °C the Au-MNM and Ag-MNM are observed to exhibit ~16 and ~20 times higher response magnitude toward Hg^0 vapor concentration of 3.26 mg/m^3 than their control counterparts, respectively. This increase is much greater than the expected increase as a result of the increased surface area (which was ~4.6 times that of the corresponding control). As well as the increase in surface area, the increase in response magnitude could also be due to the way the metals deposit on the underlying spherical PSNS. As shown in the Supporting Information, Figure S1, because of the curving nature of the PSNS, the deposited metal film topology is significantly different from that of the "flat" control thin films; thus, the curvy nature of the underlying PSNS may have created sites with high Hg^0 affinity during metal deposition. Other factors that may also play a role for the enhanced affinity of the MNM based surfaces toward Hg^0 vapor (and could change by altering these parameters) are postulated to be the interparticle PSNS gaps, the size, and shape of the underlying structure as well as the thickness of the deposited metal film. That is, our group has recently shown that the formation of surface defects can lead to

DOI: 10.1021/am507069z
ACS Appl. Mater. Interfaces 2015, 7, 1491−1499

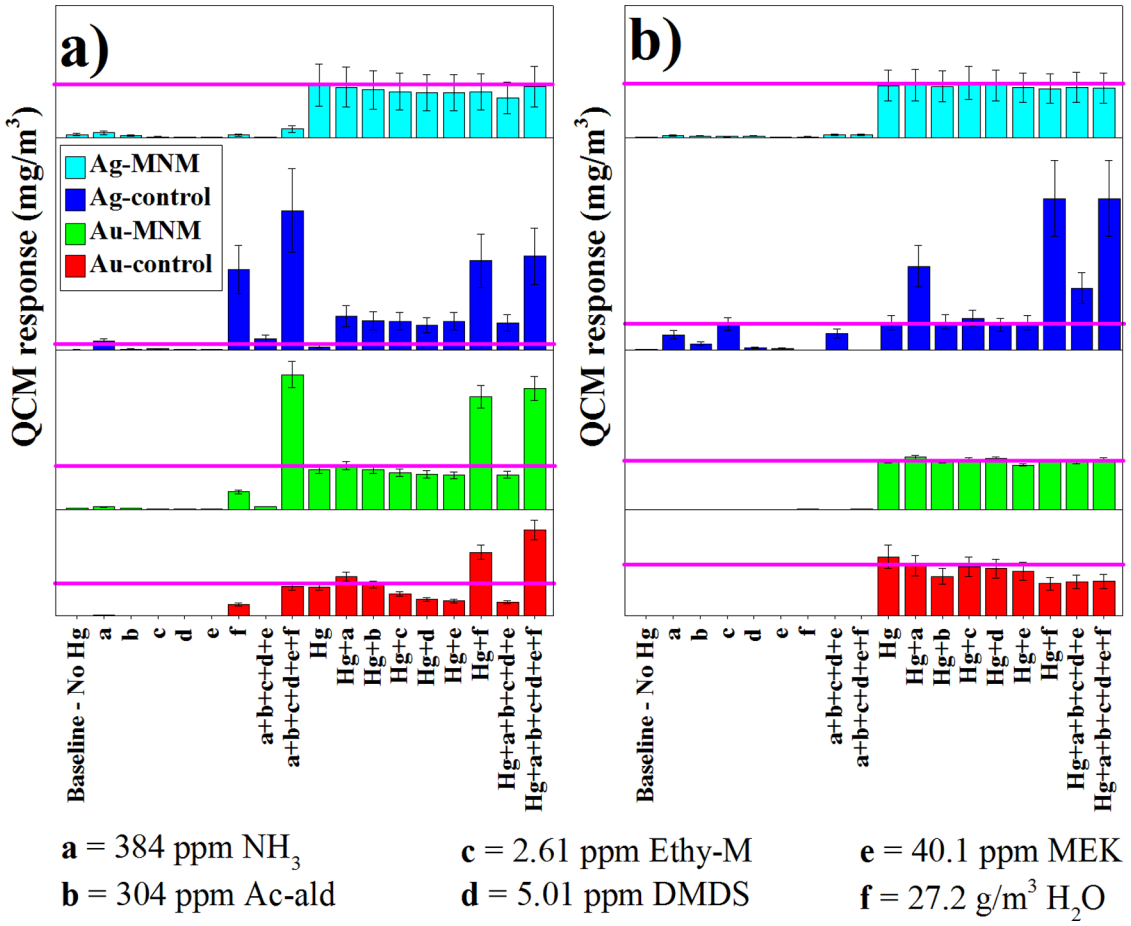

Figure 5. QCM based sensor data showing the accuracy (selectivity) performance of Au-MNM and Ag-MNM over their control counterparts when exposed to interferent gases at an operating temperature of (a) 30 °C and (b) 75 °C. The solid magenta lines in each panel represent the tested Hg^0 vapor concentration of 3.26 mg/m^3. Compared to all sensors presented, Au-MNM is observed to report the target concentration of 3.26 mg/m^3 with high accuracy and repeatability at 75 °C.

active sites that enable metal sorption to occur.[58] These surface defects can sometimes be highly active toward metal sorption where thermodynamically such sorption capacity is forbidden on otherwise polished films. In addition to this phenomenon possibly increasing the affinity of the surface toward Hg^0 vapor, it is well accepted that the presence of defect sites (crystal lattice as well as surface topology defects) increases the affinity of noble metal surfaces toward Hg^0 vapor.[31,59−62] Thus, it may be the combination of these phenomena occurring on the MNM based surfaces that results in higher sorption capacity of the noble metal layer toward Hg^0 vapor. The higher Hg^0 sorption capacity of the Au-MNM and Ag-MNM demonstrates that PCs do not just have enhanced optical properties, as has been reported thus far, but also can be designed to improve the detection properties in chemical microsensors such as QCMs where the sensing mechanism is not based on the interaction of light with the substrate.

A closer analysis of Figure 4a2 and Figure 4b2 reveals that the difference in response magnitude between the modified QCMs and their control counterparts is reduced to 2 and 6 times for Au-MNM and Ag-MNM at the operating of 75 °C, respectively. This is postulated to be due to the increased vapor pressure of Hg^0 at 75 °C relative to 30 °C, resulting in the lower tendency of the atoms to undergo sorption processes on the sensor surface. The drift of the sensors overall however is observed to reduce at the high operating temperature of 75 °C relative to 30 °C (Figure 4-a1 and Figure 4b1) but with the compromise of reduced sensitivity. The lower drift observed from the Au based QCMs is attributed to better Hg^0 desorption from the Au over the Ag surface during the 1 h recovery period where a 200 sccm dry nitrogen flow was employed following each mercury exposure.

In order to determine the detection limit of the developed sensors, the method of 3 standard deviations of the blank sample noise profile (over a 1 h period) was used. It was found that the detection limits of the modified QCMs (Au-MNM and Ag-MNM) were significantly lower than their control counterparts at 30 °C with the Au-MNM, Au-control, Ag-MNM, and Ag-control based QCMs having detection limits (LoD) of 15, 269, 21, and 307 μg/m^3, respectively. When the operating temperature was increased to 75 °C, the LoD values for the Au-MNM, Au-control, Ag-MNM, and Ag-control based QCMs were calculated to be 130, 150, 139, and 224 μg/m^3, respectively. The data suggest that the detection limit of the sensors deteriorates with increasing operating temperature; however, the modified sensors maintain their better detection limit overall. The advantage of the higher operating temperature of 75 °C is the better recovery of the sensor surfaces following a sensing event relative to 30 °C as can be observed by comparing Figure 4a1 with Figure 4b1. The extent of sensor recovery for the Au-MNM, Au-control, Ag-MNM, and Ag-control based QCMs following each Hg^0 vapor sensing event at

DOI: 10.1021/am507069z
ACS Appl. Mater. Interfaces 2015, 7, 1491−1499

Table 1. Sensor Characteristics Including Response Time (t_{90}), Detection Limit (LoD), Recovery, Accuracy, Repeatability, and Average Error As Calculated from the Data Presented in Figures 4 and 5[a]

	30 °C				75 °C			
	Au-MNM	Ag-MNM	Au-ctrl	Ag-ctrl	Au-MNM	Ag-MNM	Au-ctrl	Ag-ctrl
t_{90} (min)	46	50	42	51	29	45	24	30
LoD ($\mu g/m^3$)	15	21	269	307	130	139	149	224
recovery (%)	62	51	58	31	92	80	91	53
accuracy (%)	12	70	18	3	97	97	45	39
repeatability (%)	29	87	32	5	84	83	75	33
average error, σ (mg/m^3)	0.33	1.30	0.65	0.98	0.10	0.98	0.65	0.82

[a]The data are calculated from the sensors' response when exposed to Hg^0 vapor concentrations of 3.26 mg/m^3.

30 °C was found to be 55%, 55%, 50%, and 25%, respectively. At 75 °C, however, these values were observed to increase to 90%, 90%, 80%, and 45%, respectively. Overall it could be deduced that following any Hg^0 vapor sensing event, Au films had superior recovery properties relative to that of Ag films, which resulted in the large baseline drift observed for the Ag based QCMs during Hg^0 vapor detection experiments.

The selectivity of the developed Au-MNM and Ag-MNM based QCMs was tested by exposing them to a Hg^0 vapor concentration of 3.26 mg/m^3 in the presence of six interferent gases including ammonia (384 ppm), acetaldehyde (304 ppm), ethyl mercaptan (2.61 ppm), dimethyl disulfide (5.01 ppm), methyl ethyl ketone (40.1 ppm), and humidity (27.2 g/m^3) as well as a mixture of each. These experiments were performed on separate occasions at both 30 and 75 °C, the data of which are presented in Figure 5a and Figure 5b, respectively. In order to understand how selective the sensors are toward Hg^0 vapor in the presence of interferent gases, it is necessary to calculate the sensors' accuracies toward reporting Hg^0 vapor concentrations. This was achieved by using the data in Figure 4 to fit a calibration curve which enabled the sensor frequency output to be correlated to the exposed Hg^0 vapor concentrations. These calibration curves were also used to estimate the reported Hg^0 vapor concentrations following a sensing event when Hg^0 vapor was in the presence of interferent gases (Figure 5). The sensor response (Δf) data were found to fit well with the three-parameter loading ratio correlation (LRC) equation[63,64] given as

$$\Delta f = \frac{\Delta f_m \beta C^\eta}{1 + \beta C^\eta}$$

Here, Δf_m, β, and η are the LRC model constants. It was found that the coefficient of determination (R^2) values for the control and modified sensors when fitting the LRC equation were >0.97 and >0.99, respectively. The sensor characteristics calculated from the data presented in Figure 4 and Figure 5 are summarized in Table 1. It can be observed that at 30 °C, the modified sensors' performance was better over their control counterparts. The Au-MNM and Ag-MNM had much lower LoD, higher accuracy (when the tolerance is set at ±25%), and higher recovery than their control counterparts. In addition, the Ag-MNM had a better precision (repeatability) over the Au-MNM, which can also be graphically observed from the data presented in Figure 5a. The repeatability of the sensors was determined by first calculating the coefficient of variance (CoV) as has been described in our earlier work.[31] The accuracy and repeatability of the modified sensors (Au-MNM in particular) improved significantly when the operating temperature was raised to 75 °C. Although Au-MNM and Ag-MNM were found to have a similar repeatability (~83%) and accuracy (97%), the Au-MNM was found to have a relatively better recovery, detection limit, and response time (t_{90}) when reporting the tested Hg^0 vapor concentration of 3.26 mg/m^3 at 75 °C (Figure 5b). The Au-control and Ag-control based QCMs were observed to have low accuracy, high detection limits, and low response magnitudes toward Hg^0 vapor, making them unusable for real-world applications. It was found that although Ag-MNM had higher response magnitude, the Au-MNM, among all the sensors tested, had an overall better performance. This result has been deduced because of the high sensor recovery and confidence level (low average error (error bars)) of Au-MNM relative to Ag-MNM at 75 °C.

In order to better understand the reason behind the inaccuracy and low repeatability of the Ag-MNM based QCM, SEM and XPS analyses of the surfaces were performed following the 25-day continuous Hg^0 vapor sensing experiments, as are shown in Figure 6. The XPS data for Au-MNM

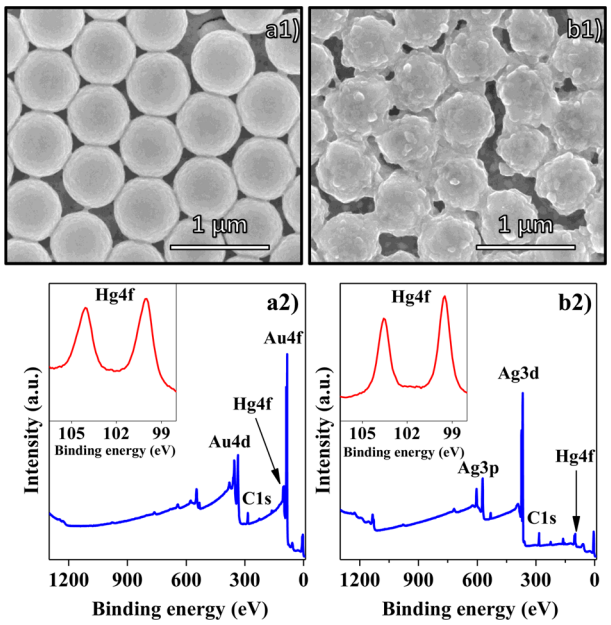

Figure 6. SEM images representing (a1) close-packed Au-MNM and (b1) close-packed Ag-MNM. XPS data of (a2) Au-MNM and (b2) Ag-MNM after Hg^0 vapor sensing experiments.

(Figure 6a2) and Ag-MNM (Figure 6b2) confirm that mercury has amalgamated with both of the developed metallic surfaces. The XPS data with detailed peak fitting are provided in the Supporting Information, Figure S2, the analysis of which revealed that Ag-MNM contained more mercury content (8.02% Hg and 91.98% Ag) relative to Au-MNM which had

DOI: 10.1021/am507069z
ACS Appl. Mater. Interfaces 2015, 7, 1491−1499

mercury content of 6.21% following Hg^0 sensing experiments. Furthermore, the XPS spectra of Ag-MNM presented in Figure S2a show that partial oxidation of Ag had occurred on the surface because of the high reactivity of the silver with oxygen. The main peak for Ag $3d_{5/2}$ appearing at the binding energy of 368.4 eV corresponds to the elemental Ag^0 form.[65] Au $4f_{7/2}$ core level appeared at the binding energy of 84.4 eV which confirmed that the Au_MNM surface contained only Au^0.[62] After mercury sensing experiments, no significant shifting of Ag 3d and Au 4f core levels was observed. Furthermore, the Hg $4f_{7/2}$ peaks in both silver and gold samples appeared around 100.4 eV which is related to the existence of elemental mercury.[66] On the basis of these results, it can be deduced that mercury had amalgamated with both the Au-MNM and Ag-MNM sensing layers. The SEM images for Au-MNM and Ag-MNM following the 25-day testing period are shown in Figure 6a1 and Figure 6b1, respectively. It can be seen that the Au-MNM, as opposed to Ag-MNM, had kept its structural integrity following the Hg^0 vapor testing experiments. This confirms that the low extent of recovery and high drift following Hg^0 sensing events associated with the Ag-MNM were due to the retaining of mercury on the Ag structures. Therefore, the relatively higher mercury content in the Ag-MNM and subsequently higher amalgam formation had resulted in the gradual change on the sensor topology. These phenomena make Ag based QCMs impractical for long-term Hg^0 vapor sensing applications. Overall, by considering the sensitivity, selectivity, recovery, and stability performance of the sensors tested, Au-MNM based Hg^0 vapor sensor can potentially be used for real-world Hg^0 vapor sensing applications.

4. CONCLUSIONS

To summarize, we have shown for the first time that although photonic crystal (PC) based Au (Au-MNM) and Ag (Ag-MNM) nanostructures are well-known for their optical properties, they can additionally be employed for nonoptical based chemical sensing applications. To demonstrate this, the Au-MNM and Ag-MNM nanostructures were deposited on quartz crystal microbalance (QCM) transducers and used to selectively detect low concentrations of Hg^0 vapor in the presence of interferent gases. The Au-MNM and Ag-MNM exhibited extremely high sensitivity (~16 and ~20 times, respectively) and much lower detection limits (<3 ppb_v and <15 ppb_v) toward Hg^0 vapor relative to their control counterparts (>30 ppb_v and >17 ppb_v) at 30 and 75 °C, respectively. At 75 °C, The Au-MNM was found to outperform the Ag-MNM because of its lower drift, high accuracy, and recovery as well as better selectivity toward Hg^0 vapor, thus making it suitable to be used as an online Hg^0 vapor sensor in many mercury emitting industries.

■ ASSOCIATED CONTENT

Supporting Information

SEM images of Au-control and Au-MNM and X-ray photoemission spectra of Ag-MNM. This material is available free of charge via the Internet at http://pubs.acs.org.

■ AUTHOR INFORMATION

Corresponding Author

*E-mail: suresh.bhargava@rmit.edu.au. Phone: +61 3 99252330.

Author Contributions

†Y.M.S. and A.E.K. have equal contribution.

All authors have contributed substantially to this work. S.K.B. supervised the research. Y.M.S., A.E.K., and S.J.I. have conducted the experiments. All authors analyzed the data and reviewed the manuscript.

Notes

The authors declare no competing financial interest.

■ ACKNOWLEDGMENTS

The authors acknowledge the Australian Research Council (ARC) for supporting this project (Grant LP100200859) and the RMIT Microscopy and Microanalysis Facility (RMMF) for allowing the use of their comprehensive facilities and services. A.E.K. acknowledges RMIT's College of Science, Engineering and Health (SEH) for financial support through the Higher Degree by Research Publications Grant (HDRPG).

■ REFERENCES

(1) Alivisatos, A. P. Semiconductor Clusters, Nanocrystals, and Quantum Dots. *Science* **1996**, *271*, 933−937.

(2) Wu, Y.; Dong, N.; Fu, S.; Fowlkes, J. D.; Kondic, L.; Vincenti, M. A.; de Ceglia, D.; Rack, P. D. Directed Liquid Phase Assembly of Highly Ordered Metallic Nanoparticle Arrays. *ACS Appl. Mater. Interface* **2014**, *6*, 5835−5843.

(3) Duan, H.; Wang, D.; Kurth, D. G.; Möhwald, H. Directing Self-Assembly of Nanoparticles at Water/Oil Interfaces. *Angew. Chem., Int. Ed.* **2004**, *43*, 5639−5642.

(4) Huang, J.; Tao, A. R.; Connor, S.; He, R.; Yang, P. A General Method for Assembling Single Colloidal Particle Lines. *Nano Lett.* **2006**, *6*, 524−529.

(5) Glotzer, S. C.; Solomon, M. J.; Kotov, N. A. Self-Assembly: From Nanoscale to Microscale Colloids. *AIChE J.* **2004**, *50*, 2978−2985.

(6) Kamiko, M.; Suenaga, R.; Koo, J.-W.; Nose, K.; Kyuno, K.; Ha, J.-G. Effect of Ti Seed Layers on Structure of Self-Organized Epitaxial Face-Centered-Cubic-Ag(001) Oriented Nanodots. *J. Appl. Phys.* **2013**, *114*, 244307.

(7) Lian, J.; Wang, L.; Sun, X.; Yu, Q.; Ewing, R. C. Patterning Metallic Nanostructures by Ion-Beam-Induced Dewetting and Rayleigh Instability. *Nano Lett.* **2006**, *6*, 1047−1052.

(8) Hicks, E. M.; Zou, S.; Schatz, G. C.; Spears, K. G.; Van Duyne, R. P.; Gunnarsson, L.; Rindzevicius, T.; Kasemo, B.; Käll, M. Controlling Plasmon Line Shapes through Diffractive Coupling in Linear Arrays of Cylindrical Nanoparticles Fabricated by Electron Beam Lithography. *Nano Lett.* **2005**, *5*, 1065−1070.

(9) Xia, L.; Yang, Z.; Yin, S.; Guo, W.; Li, S.; Xie, W.; Huang, D.; Deng, Q.; Shi, H.; Cui, H.; Du, C. Surface Enhanced Raman Scattering Substrate with Metallic Nanogap Array Fabricated by Etching the Assembled Polystyrene Spheres Array. *Opt. Express* **2013**, *21*, 11349−11355.

(10) Geng, C.; Zheng, L.; Yu, J.; Yan, Q.; Wei, T.; Wang, X.; Shen, D. Thermal Annealing of Colloidal Monolayer at the Air/Water Interface: A Facile Approach to Transferrable Colloidal Masks with Tunable Interstice Size for Nanosphere Lithography. *J. Mater. Chem.* **2012**, *22*, 22678−22685.

(11) Farzinpour, P.; Sundar, A.; Gilroy, K. D.; Eskin, Z. E.; Hughes, R. A.; Neretina, S. Dynamic Templating: A Large Area Processing Route for the Assembly of Periodic Arrays of Sub-Micrometer and Nanoscale Structures. *Nanoscale* **2013**, *5*, 1929−1938.

(12) Tsvetkov, M. Y.; Khlebtsov, B.; Khanadeev, V.; Bagratashvili, V.; Timashev, P.; Samoylovich, M.; Khlebtsov, N. SERS Substrates Formed by Gold Nanorods Deposited on Colloidal Silica Films. *Nanoscale Res. Lett.* **2013**, *8*, 250.

(13) González-Urbina, L.; Baert, K.; Kolaric, B.; Pérez-Moreno, J.; Clays, K. Linear and Nonlinear Optical Properties of Colloidal Photonic Crystals. *Chem. Rev.* **2012**, *112*, 2268−2285.

DOI: 10.1021/am507069z
ACS Appl. Mater. Interfaces 2015, 7, 1491−1499

(14) Ruminski, A. M.; Barillaro, G.; Chaffin, C.; Sailor, M. J. Internally Referenced Remote Sensors for HF and Cl_2 Using Reactive Porous Silicon Photonic Crystals. *Adv. Funct. Mater.* **2011**, *21*, 1511−1525.
(15) Ye, Y.-H.; Mayer, T. S.; Khoo, I.-C.; Divliansky, I. B.; Abrams, N.; Mallouk, T. E. Self-Assembly of Three-Dimensional Photonic-Crystals with Air-Core Line Defects. *J. Mater. Chem.* **2002**, *12*, 3637−3639.
(16) Galisteo-López, J. F.; Ibisate, M.; Sapienza, R.; Froufe-Pérez, L. S.; Blanco, Á.; López, C. Self-Assembled Photonic Structures. *Adv. Mater.* **2011**, *23*, 30−69.
(17) Fenzl, C.; Hirsch, T.; Wolfbeis, O. S. Photonic Crystals for Chemical Sensing and Biosensing. *Angew. Chem., Int. Ed.* **2014**, *53*, 3318−3335.
(18) Alonso-González, P.; Albella, P.; Schnell, M.; Chen, J.; Huth, F.; García-Etxarri, A.; Casanova, F.; Golmar, F.; Arzubiaga, L.; Hueso, L. E.; Aizpurua, J.; Hillenbrand, R. Resolving the Electromagnetic Mechanism of Surface-Enhanced Light Scattering at Single Hot Spots. *Nat. Commun.* **2012**, *3*, 684.
(19) Zhang, N.; Liu, Y. J.; Yang, J.; Su, X.; Deng, J.; Chum, C. C.; Hong, M.; Teng, J. High Sensitivity Molecule Detection by Plasmonic Nanoantennas with Selective Binding at Electromagnetic Hotspots. *Nanoscale* **2014**, *6*, 1416−1422.
(20) Drelich, J.; White, C. L.; Xu, Z. Laboratory Tests on Mercury Emission Monitoring with Resonating Gold-Coated Silicon Cantilevers. *Environ. Sci. Technol.* **2008**, *42*, 2072−2078.
(21) Mirsky, V. M.; Vasjari, M.; Novotny, I.; Rehacek, V.; Tvarozek, V.; Wolfbeis, O. S. Self-Assembled Monolayers as Selective Filters for Chemical Sensors. *Nanotechnology* **2002**, *13*, 175−178.
(22) McNerney, J. J.; Buseck, P. R.; Hanson, R. C. Mercury Detection by Means of Thin Gold Films. *Science* **1972**, *178*, 611−612.
(23) McNicholas, T. P.; Zhao, K.; Yang, C.; Hernandez, S. C.; Mulchandani, A.; Myung, N. V.; Deshusses, M. A. Sensitive Detection of Elemental Mercury Vapor by Gold-Nanoparticle-Decorated Carbon Nanotube Sensors. *J. Phys. Chem. C* **2011**, *115*, 13927−13931.
(24) Ramesh, G. V.; Radhakrishnan, T. P. A Universal Sensor for Mercury (Hg, Hg^{I}, Hg^{II}) Based on Silver Nanoparticle-Embedded Polymer Thin Film. *ACS Appl. Mater. Interfaces* **2011**, *3*, 988−994.
(25) Qui, J. Tough Talk over Mercury Treaty. *Nature* **2013**, *493*, 144−145.
(26) Gardner, E. Peru Battles the Golden Curse of Madre de Dios. *Nature* **2012**, *486*, 306−307.
(27) Xu, L.; Liu, N.; Cao, Y.; Lu, F.; Chen, Y.; Zhang, X.; Feng, L.; Wei, Y. Mercury Ion Responsive Wettability and Oil/Water Separation. *ACS Appl. Mater. Interfaces* **2014**, *6*, 13324−13329.
(28) Canstein, H. V.; Kelly, S.; Li, Y.; Wagner-Dobler, I. Species Diversity Improves the Efficiency of Mercury-Reducing Biofilms under Changing Environmental Condtions. *Appl. Environ. Microbiol.* **2002**, *68*, 2829−2837.
(29) Schrope, M. US To Take Temperature of Mercury Threat. *Nature* **2001**, *409*, 124−124.
(30) Laudal, D. L.; Thompson, J. S.; Pavlish, J. H.; Brickett, L. A.; Chu, P. Use of Continuous Mercury Monitors at Coal-Fired Utilities. *Fuel Process. Technol.* **2004**, *85*, 501−511.
(31) Sabri, Y. M.; Ippolito, S. J.; O'Mullane, A. P.; tardio, J.; Bansal, V.; Bhargava, S. Creating Gold Nanoprisms Directly on Quartz Crystal Microbalance Electrodes for Mercury Vapor Sensing. *Nanotechnology* **2011**, *22*, 305501−09.
(32) Sholupov, S.; Pogarev, S.; Ryzhov, V.; Mashyanov, N.; Stroganov, A. Zeeman Atomic Absorption Spectrometer RA-915+ for Direct Determination of Mercury in Air and Complex Matrix Samples. *Fuel Process. Technol.* **2004**, *85*, 473−485.
(33) Logar, M.; Horvat, M.; Akagi, H.; Pihlar, B. Simultaneous Determination of Inorganic Mercury and Methylmercury Compounds in Natural Waters. *Anal. Bioanal. Chem.* **2002**, *374*, 1015−1021.
(34) Battistoni, C.; Bemporad, E.; Galdikas, A.; Kaciulis, S.; Mattogno, G.; Mickevicius, S.; Olevano, V. Interaction of Mercury Vapour with Thin Films of Gold. *Appl. Surf. Sci.* **1996**, *103*, 107−111.
(35) Keller, L. O.; Kallis, K. T.; Fieldler, H. L. Nano-Fin Based Mercury-Sensor for Environmental Surveillance. *J. Nanosci. Nanotechnol.* **2010**, *10*, 5921−5925.
(36) James, J. Z.; Lucas, D.; Koshland, C. P. Gold Nanoparticle Films as Sensitive and Reusable Elemental Mercury Sensors. *Environ. Sci. Technol.* **2012**, *46*, 9557−9562.
(37) Unciti-Broceta, A.; Johansson, E. M. V.; Yusop, R. M.; Sanchez-Martin, R. M.; Bradley, M. Synthesis of Polystyrene Microspheres and Functionalization with Pd^0 Nanoparticles To Perform Bioorthogonal Organometallic Chemistry in Living Cells. *Nat. Protoc.* **2012**, *7*, 1207−1218.
(38) Sauerbrey, G. Verwendung Von Schwingquarzen Zur Wägung Dünner Schichten Und Zur Mikrowägung. *Z. Phys.-e.A: Hadrons Nucl.* **1959**, *155*, 206−222.
(39) Sabri, Y. M.; Ippolito, S. J.; Atanacio, A. J.; Bansal, V.; Bhargava, S. K. Mercury Vapor Sensor Enhancement by Nanostructured Gold Deposited on Nickel Surfaces Using Galvanic Replacement Reactions. *J. Mater. Chem.* **2012**, *22*, 21395−21404.
(40) Sabri, Y. M.; Kojima, R.; Ippolito, S. J.; Wlodarski, W.; Kalantar-zadeh, K.; Kaner, R. B.; Bhargava, S. K. QCM Based Mercury Vapor Sensor Modified with Polypyrrole Supported Palladium. *Sens. Actuators, B* **2011**, *160*, 616−622.
(41) Oh, J. R.; Moon, J. H.; Yoon, S.; Park, C. R.; Do, Y. R. Fabrication of Wafer-Scale Polystyrene Photonic Crystal Multilayers via the Layer-by-Layer Scooping Transfer Technique. *J. Mater. Chem.* **2011**, *21*, 14167−14172.
(42) Rand, D. A. J.; Woods, R. The Nature of Adsorbed Oxygen on Rhodium, Palladium and Gold Electrodes. *J. Electroanal. Chem.* **1971**, *31*, 29−38.
(43) Levlin, M.; Niemi, H. E. M.; Hautojärvi, P.; Ikävalko, E.; Laitinen, T. Mercury Adsorption on Gold Surfaces Employed in the Sampling and Determination of Vaporous Mercury: A Scanning Tunneling Microscopy Study. *Fresenius' J. Anal. Chem.* **1996**, *355*, 2−9.
(44) Zeng, H.; Xu, X.; Bando, Y.; Gautam, U. K.; Zhai, T.; Fang, X.; Liu, B.; Golberg, D. Template Deformation-Tailored ZnO Nanorod/Nanowire Arrays: Full Growth Control and Optimization of Field-Emission. *Adv. Funct. Mater.* **2009**, *19*, 3165−3172.
(45) Bilic, A.; Reimers, J. R.; Hush, N. S.; Hafner, J. Adsorption of Ammonia on the Gold (111) Surface. *J. Chem. Phys.* **2002**, *116*, 8981−8987.
(46) Tanida, K.; Hoshino, M. Contiuous Determination of Mercury in Air by Gold Amalgamation and Flameless. *Rigaku J.* **1990**, *7*, 35−40.
(47) Finklea, H. O.; Avery, S.; Lynch, M.; Furtsch, T. Blocking Oriented Monolayers of Alkyl Mercaptans on Gold Electrodes. *Langmuir* **2002**, *3*, 409−413.
(48) Rocha, T. A. P.; Gomes, M. T. S. R.; Duarte, A. C.; Oliveira, J. A. B. P. Quartz Crystal Microbalance with Gold Electrodes as a Sensor for Monitoring Gas-Phase Adsorption/Desorption of Short Chain Alkylthiol and Alkyl Surfides. *Anal. Commun.* **1998**, *35*, 415−416.
(49) Richton, R. E.; Farrow, L. A. Adsorption Kinetics of Ammonia on an Inhomogeneous Gold Surface. *J. Phys. Chem.* **1981**, *85*, 3577−3581.
(50) Kay, B. D.; Lykke, K. R.; Creighton, J. R.; Ward, S. J. The Influence of Adsorbate—Absorbate Hydrogen Bonding in Molecular Chemisorption: NH_3, HF, and H_2O on Au(111). *J. Chem. Phys.* **1989**, *91*, 5120−5121.
(51) Surplice, N. A.; Brearley, W. The Adsorption of Carbon Monoxide, Ammonia, and Wet Air on Gold. *Surf. Sci.* **1975**, *52*, 62−74.
(52) Nuss, H.; Jansen, M. $[Rb([18]Crown\text{-}6)(NH_3)_3]Au.NH_3$: Gold as Acceptor in N-H···Au^- Hydrogen Bonds. *Angew. Chem., Int. Ed.* **2006**, *45*, 4369−4371.
(53) de Vooys, A. C. A.; Mrozek, M. F.; Koper, M. T. M.; van Santen, R. A.; van Veen, J. A. R.; Weaver, M. J. The Nature of Chemisorbates Formed from Ammonia on Gold and Palladium Electrodes As Discerned from Surface-Enhanced Raman Spectroscopy. *Electrochem. Commun.* **2001**, *3*, 293−298.
(54) Meyer, R.; Lemire, C.; Shaikhutdinov, S. K.; Freund, H. Surface Chemistry of Catalysis by Gold. *Gold Bull.* **2004**, *37*, 72−124.

DOI: 10.1021/am507069z
ACS Appl. Mater. Interfaces 2015, 7, 1491−1499

(55) Mullett, M.; Tardio, J.; Bhargava, S.; Dobbs, C. Removal of Mercury from an Alumina Refinery Aqueous Stream. *J. Hazard. Mater.* **2007**, *144*, 274−282.
(56) Wu, C. Y.; Huang, C. C.; Jhang, J. S.; Liu, A. C.; Chiang, C.-C.; Hsieh, M.-L.; Huang, P.-J.; Tuyen, L. D.; Minh, L. Q.; Yang, T. S.; Chau, L.-K.; Kan, H.-C.; Hsu, C. C. Hybrid Surface-Enhanced Raman Scattering Substrate from Gold Nanoparticle and Photonic Crystal: Maneuverability and Uniformity of Raman Spectra. *Opt. Express* **2009**, *17*, 21522−21529.
(57) Kong, K. V.; Leong, W. K.; Lam, Z.; Gong, T.; Goh, D.; Lau, W. K. O.; Olivo, M. A Rapid and Label-Free SERS Detection Method for Biomarkers in Clinical Biofluids. *Small* **2014**, *10*, 5030−5034.
(58) Plowman, B. J.; Field, M. R.; Bhargava, S. K.; O'Mullane, A. P. Exploiting the Facile Oxidation of Evaporated Gold Films To Drive Electroless Silver Deposition for the Creation of Bimetallic Au/Ag Surfaces. *ChemElectroChem* **2014**, *1*, 76−82.
(59) George, M. A.; Glaunsinger, W. S. The Electrical and Structural Properties of Gold Films and Mercury-Covered Gold Films. *Thin Solid Films* **1994**, *245*, 215−224.
(60) Sabri, Y. M.; Ippolito, S. J.; Tardio, J.; Atanacio, A. J.; Sood, D. K.; Bhargava, S. K. Mercury Diffusion in Gold and Silver Thin Film Electrodes on Quartz Crystal Microbalance Sensors. *Sens. Actuators, B* **2009**, *137*, 246−252.
(61) Sabri, Y. M.; Ippolito, S. J.; Tardio, J.; Bhargava, S. K. Study of Surface Morphology Effects on Hg Sorption-Desorption Kinetics on Gold Thin-Films. *J. Phys. Chem. C* **2012**, *116*, 2483−2492.
(62) Sabri, Y. M.; Ippolito, S. J.; Tardio, J.; Bansal, V.; O'Mullane, A. P.; Bhargava, S. K. Gold Nanospikes Based Microsensor as a Highly Accurate Mercury Emission Monitoring System. *Sci. Rep.* **2014**, *4*, 6741−6748.
(63) Yao, C. Extended and Improved Langmuir Equation for Correlating Adsorption Equilibrium Data. *Sep. Purif. Technol.* **2000**, *19*, 237−242.
(64) Kapoor, A.; Ritter, J. A.; Yang, R. T. An Extended Langmuir Model for Adsorption of Gas Mixtures on Heterogeneous Surfaces. *Langmuir* **1990**, *6*, 660−664.
(65) Kandjani, A. E.; Mohammadtaheri, M.; Thakkar, A.; Bhargava, S. K.; Bansal, V. Zinc Oxide/Silver Nanoarrays as Reusable SERS Substrates with Controllable "Hot-Spots" for Highly Reproducible Molecular Sensing. *J. Colloid Interface Sci.* **2014**, *436*, 251−257.
(66) Sumesh, E.; Bootharaju, M. S.; Anshup; Pradeep, T. A Practical Silver Nanoparticle-Based Adsorbent for the Removal of Hg^{2+} from Water. *J. Hazard. Mater.* **2011**, *189*, 450−457.

DOI: 10.1021/am507069z
ACS Appl. Mater. Interfaces 2015, 7, 1491−1499